

# Leveraging On-Chip Transistor Switching for Communication and Sensing in Neural Implants and Gastrointestinal Devices

Seun Sangodoyin, *Member, IEEE*, Elvan M. Ugurlu, *Student Member, IEEE*, Moumita Dey, *Student Member, IEEE*, Milos Prvulovic, *Senior Member, IEEE* and Alenka Zajić, *Senior Member, IEEE*

**Abstract—Objective:** This paper presents a Proof-of-Concept (POC) design and implementation of a biosensing and communication system that can be used for biotelemetry in neural and Gastrointestinal (GI) applications. **Methods:** Our proposed system is based on backscattering from a semi-passive Radio-Frequency-Identification-Device (RFID) implemented using an Application Specific Integrated Circuit (ASIC) in which electronic switching between transistor gates in high and low states create an impedance difference, thereby effectively changing the ASIC's Radar Cross Section (RCS) and thus modulating its backscattered field. The ASIC is used in conjunction with a biosensor to measure and transmit vital signs from within the body. With this system, we conducted backscatter propagation experiments through different biological and phantom tissues (in *ex-vivo* and *in-vitro*) in the GI and neural environments. **Results:** Our results show that the backscattered waveforms can penetrate tissues of various compositions and thicknesses with power received at distances of up to 55 cm away from the RFID ASIC. Furthermore, results from single- and multi-bit biotelemetry measurements showed a high signal fidelity with low Bit-Error-Rate (BER) while being able to resolve varying tissue temperatures measured by the biosensor in our system. **Conclusion:** We realized a POC system in which on-chip transistor switching in an ASIC can be used to achieve backscatter communication and biosensing. This system is deployable in neural and GI applications. **Significance:** Our findings in this work will provide an important practical basis for the design and development of RFID ASIC for biosensing and biotelemetry in medical applications.

**Index Terms—**Bioelectronics, Backscatter communication, biotelemetry, implantable devices, propagation channel model.

## I. INTRODUCTION

INCREASING advancement in bioelectronics research for physiological monitoring has led to numerous discoveries and deployment of biomedical devices in the human body with applications in the neural and gastrointestinal systems. Gastrointestinal (GI) devices such as smart endoscopic capsules are being used in imaging the GI tracts for diagnosis of conditions like Crohn's diseases, Obscure Gastrointestinal Bleeding (OGIB), celiac disease, and polyposis syndrome [1], while gastric residence devices perform tasks such as pH level measurement [2] and long-term drug delivery [3].

S. Sangodoyin, E. M. Ugurlu, M. Dey, and A. Zajić are with the School of Electrical and Computer Engineering, Georgia Institute of Technology, Atlanta, GA 30332-0250 USA (email: {seun.sangodoyin; ugurlu; mdey}@gatech.edu, alenka.zajic@ece.gatech.edu).

Milos Prvulovic is with the School of Computer Science, Georgia Institute of Technology, Atlanta, Georgia 30332-0250 USA (email: milos@cc.gatech.edu)

Neural implants are being used for neuromodulation methods such as Deep Brain Stimulation (DBS) [4] to treat epilepsy, Parkinson's disease, dystonia and tinnitus while hippocampal neural prosthetic implants have found use in the restoration and improvement of memory functions in the human brain [5].

In order to analyze the vital medical information gathered using such sensors within the body and subsequently perform diagnosis, this medical information needs to be transmitted to another device outside of the body. This is usually accomplished with the aid of a wireless chip transmitter embedded in the biomedical implant (bioimplant), or via tethering, which involves the use of a wire that, in the case of neural implants, can pass through a drilled hole in the cranium. The tethered approach is often inconvenient for patients, while the problem with the wireless alternative is low power requirement and lack of design flexibility. The use of batteries for powering the bioimplant is usually a concern as it suffers weight, size, safety, and biocompatibility issues. For example, in an endoscopic capsule, half of the energy required for its operation is often expended on Radio-Frequency (RF) transmission [6]. This gets worse when conducting other tasks such as sensing, conducting, drug delivery, and mechanical actuation. The aforementioned tasks have enormous power demands.

Recently, several ideas have been proposed to obviate the need for or limit the use of batteries in bioimplants. These ideas range from externally powering the devices [7]–[13] to using power harvesting technique in the GI tract [14] and the deployment of passive/semi-passive Radio-Frequency Identification (RFID) backscatter communication devices [6], [15], [16]. The concept of backscatter communication is particularly attractive due to its simplicity as it involves a transmitting device (known as a *reader* or *interrogator*) sending a continuous waveform, which is modulated with information and reflected (backscattered) to the reader by a device known as the *tag*. The modulation of the continuous waveform is achieved through the input impedance associated with the tag's antenna being intentionally mismatched with two-state RF loads. This mismatch causes a variation in the tag's reflection coefficient thereby modulating the incoming continuous waveform [17]. The make-up of most wireless chip transmitters and backscattering devices in the literature can be deemed as complex due the use of a large number of components, which includes antennas, amplifiers, and front-end circuits. Furthermore, these devices lack the necessary

design flexibility (such as ad-hoc variation of the continuous waveform frequency) and versatility (in terms of single and multi-bit data rate output) options that could end up simplifying the overall biomedical device's functionality. Therefore, there is a need for a novel biotelemetry system design with low-complexity, small form factor, and low power consumption that offers the aforementioned flexibility and versatility purposed towards neural implants and gastrointestinal devices.

### A. Related Work

Several publications [6], [9], [15]–[21] have dealt with backscatter communication by using RFID implementation for various tasks. A passive RFID for patient monitoring was introduced in [18], while RFID was utilized for asset tracking in [19]. An ultrawideband (UWB) RFID tag design was presented in [20] while an active UWB reflector RFID tag, which uses a broadband amplifier to enhance its Radar-Cross-Section (RCS) for wireless sensors applications was presented in [21]. Traditional passive RFID tags were used for backscattering in bioimplants in [9], [15] and [16]. A multi-antenna approach was used for bioimplant backscattering in [6]. Although the system offered some flexibility with regards to the frequency of the incident waveform, however, the use of multiple antennas made the system complex. The concept digital electronic switching for RFID backscattering applications was presented in our previous work [17], however, all the experiments in the aforementioned reference were conducted in free-space and at high frequencies of 5.8, 17.46 and 26.5 GHz, which are not suitable for bio-centric applications.

### B. Contributions

As can be seen from the literature review above, with the exception of [17], most of the backscatter systems presented in these works are based on traditional RFID concepts. There is no low-complexity, low power consumption, flexible and versatile system available for backscattering purposes in bioimplants. We remedy this by providing a Proof-of-Concept (POC) design and implementation for a biosensing and backscatter communication system that can be used for biotelemetry in neural implants and GI applications. The novelty in our work is that unlike currently existing biotelemetry solutions, it is antenna-less; operates without amplifiers or front-end circuits; low-complexity; offers spectral flexibility in terms of modulation frequency selection and versatility in terms of choice of using single or multiple bits for communication. A comparison between our system and state-of-art biotelemetry devices has been provided in Supplementary Material 1 (i.e. SM 1). The contributions of this paper can be summarized as follows.

- 1) We provide details on an on-chip backscattering systems designed for biotelemetry and biosensing in neural and GI environments.
- 2) We provide an extensive report on a measurement campaign to study backscattering signal propagation through select biological tissues, GI and neural tissues.

- 3) We provide a propagation model along with statistical estimates of the extracted propagation channel parameters, which can be used for the computation of (received) backscattered signal power.
- 4) We provide details on biosensing and telemetry experiments conducted with single- and multi-bit data streams along with channel coding technique and data symbol detection procedure designed for this work.
- 5) We identify important limitations and provide a guidance towards future prototype development.

All the measurements conducted in this paper are either *ex-vivo* or *in-vitro* tests. Note that (biological) Porcine tissues were used for *ex-vivo* tests due to its dielectric similarity to that of humans [22], while self-developed head phantom tissues were used for the (neural) *in-vitro* tests. Given that tissues are either biological or phantom in this work, we will hence refer to the term *biomaterial* when addressing tissues in a larger context. This work provides a 'proof-of-concept' for achieving biotelemetry with transistor switching in an ASIC. It offers guidance to system designers and serves as a first step in realizing the on-chip backscattering concept in bioimplants and ingestible devices. We encourage readers to bear this in mind when interpreting the results in this paper.

### C. Organization

This paper is organized as follows. Section II describes the On-Chip backscattering system design while Section III describes the POC system design and implementation. Limitations of our work is discussed in Section IV. Section V describes the propagation measurements through tissues. Backscatter communication and sensing are discussed in Section VI while the summary and conclusions are inferred in Section VII.

## II. ON-CHIP BACKSCATTERING SYSTEM DESIGN

Traditional backscattering requires a mismatch between impedance associated with a radiating antenna element and pre-assigned load impedances. The same principle can be achieved with an Application Specific Integrated Circuit (ASIC) of digital electronic inverters made from n-type Metal-Oxide-Semiconductor (NMOS) and p-type Metal-Oxide-Semiconductor (PMOS) transistors i.e., Complementary Metal-Oxide-Semiconductor (CMOS). The CMOS inverter has two-state RF loads and can be configured to motivate the modulation of backscattered signals. The typical operation of a CMOS inverter is such that when its input voltage is low, the NMOS transistors in the inverters will be inactive (off) while the PMOS transistor will be active (on) – due to its complementary nature. This results in the existence of a direct path between the output voltage ( $V_{out}$ ) and the supply voltage ( $V_{DD}$ ) with the presence of a finite resistance – thereby motivating a high output inverter state. Conversely, a high inverter input leads to a low inverter output due to the existence of a finite resistance between the output and the ground. The CMOS transistor is used in realizing digital logic gates such as NOR and NAND gate structures, which are the basic building block for critical components in digital

electronic circuitry. The intentional switching between NAND logic’s high and low output states creates an impedance variation, which is similar to the variation in antenna terminating impedances in traditional RFID tags [17]. The aforementioned impedance variation leads to a change in the circuit’s Radar Cross Section (RCS) thereby modulating the incident signal prior to backscattering. It is important to note that since this proposed backscattering system is antenna-less, we attribute the backscattering to routing wire segments (i.e. interconnect wiring) on the ASIC. The aforementioned backscattering is achieved exclusively through reflections from the interconnect wiring in the integrated circuit and not through any form of radiation. This is a form of communication by means of reflected power as discussed in [23]. Note that radiation from interconnect wiring in a small size ASIC would have to happen at an ultrahigh frequency i.e., higher than the 915 MHz used in this work. The backscattering procedure undertaken in this work is independent of the size of the integrated circuit and the frequency of the impinging continuous waveform. This fact has also been shown in [24].

### A. Backscatter Signal Modulation Process

An FPGA chip was adopted in this work to demonstrate the use of transistor switching for backscatter communication in an ASIC. Although an extensive discourse on this technique has been presented in [17], however, to make this paper self-contained, we proceed with a brief yet concise discussion of this approach. We encourage interested readers to see ref. [17] for any additional details.

Within the FPGA chip, a Linear Feedback Shift Register (LFSR) was configured through contiguously connected flip-flops (constructed from CMOS NAND gates) as shown in Fig. 1. With respect to our work, one of the key advantages that the LFSR affords is the possibility of an extended cycle of operation – using a sequence of priorly selected patterns – as the output bit is continuously fed back to the input of the LFSR. To modulate the continuous waveform (with carrier frequency  $f_c$ ) incident on the FPGA chip, the flip-flops in the LFSR were programmed to switch patterns between a high and low state at an on-board clock frequency ( $f_{clock}$ ) rate of 50 MHz for half a cycle and then stay dormant for the other half so as to create a periodic switching cycle i.e., a modulation frequency,  $f_m$ . This oscillatory pattern can be observed in Fig. 2. From the switching cycle (with modulation frequency,  $f_m$ ), the resulting frequencies of the modulated backscattered signal can be written as  $f_c \pm f_m$ .

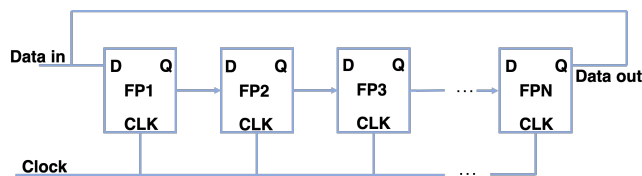


Fig. 1: Flip-flops configured into shift registers.

It is important to note that the ability to vary the modulation frequency  $f_m$  (thereby changing  $f_c \pm f_m$ ) simply by altering

the switching pattern of the flip-flops in our system showcases the flexibility that our design affords. Also, note that an increment in the number of simultaneously switched flip-flops results in a stronger backscattered waveform. From our discussion so far, it should be noted that the continuous use of a single LFSR results into backscattering at a single modulation frequency – this constitutes a high data rate single-bit operation. High data rate multi-bit outputs can be achieved by running multiple LFSRs at different rates, such that backscattered waveforms would occur at different modulation frequencies, with each modulation frequency corresponding to each data bit. This exemplifies the aforementioned versatility required in biotelemetry devices.

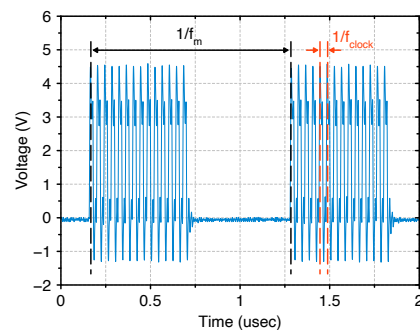


Fig. 2: Oscillatory pattern of flip-flops with  $f_m = 900$  kHz.

### B. Resource Allocation

The selection of an optimal operational mode for an ASIC (in this case the FPGA chip) is essential to its deployment in bioimplants. Hence, it suffices to consider the FPGA chip’s resource allocation options in terms of logic gate utilization percentages in conjunction with its power consumption and thermal profile. Since our ultimate objective is to describe how an ASIC embedded into a bioimplant can be used for biotelemetry through backscattering and for ease of discussion, in the rest of this paper, we will henceforth refer to the FPGA chip as a *biochip*. In this work, the task of the biochip can be divided into sensor data processing/computing and backscatter communication (as shown in Fig. 3). A bioimplant, which comprises of multiple sensors could require significant amount of data processing while needing resources (logic gates) to backscatter processed information to the interrogator. Therefore, it is only ideal that an optimal procedure to accomplish this dual functionality be investigated.

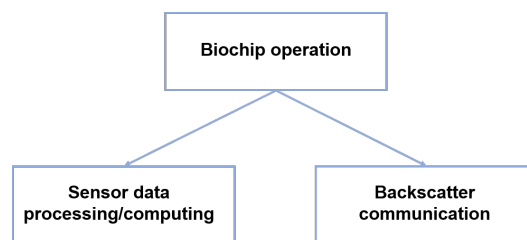


Fig. 3: Biochip task distribution.

The concept of logic utilization involves splitting the biochip’s resources into proportions such that at a maximum of 100%,  $N = 36600$  flip-flops are utilized while 70% and 40% utilization constitutes the usage of 25990 and 15155 flip-flops respectively. An illustration of the logic utilization mapping on an ALTERA Cyclone V FPGA chip used in this work has been provided in Fig. 4.

The advantages that logic utilization assignment affords includes i) improvement of the received (backscattered) signal power; ii) flexibility in on-demand assignment of additional resources to auxiliary applications such as sensor data processing; iii) indirect control of power consumption and thermal profile of the biochip. The third advantage is especially important since power consumption is usually a critical concern for most bioimplants due to the lifetime of batteries and the fact that excessive dissipation of heat could cause irreversible damage to some biological tissues.

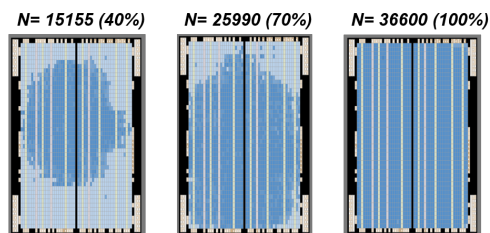


Fig. 4: Logic utilization mapping of an ALTERA Cyclone V FPGA chip.

To characterize the impact of logic utilization in terms of the signal power received, power consumed and thermal profiles, we conducted some measurements (more on this in Sec. III) with different logic utilization percentages at varying proximity distances (see Table I) between the biochip and an interrogator. A plot of the received power at the different utilization percentages and distances is shown in Fig. 5. It can be clearly observed from Fig. 5 that the received power mostly decreases with decreasing percentage utilization and increasing biochip - interrogator separation. It is important to note that choosing an optimal utilization percentage and tag - interrogator distance depends on usage plan.

TABLE I: Distances between the interrogator and tag.

Index	d1	d2	d3	d4	d5
Distances (cm)	7.5	15	25	35	55

With increased functionality (logic utilization percentage), it is expected that the power consumption by the biochip will also increase, which will in turn lead to an increase in heat generated. Results from an experiment conducted confirming this i.e., showing a monotonic (increase) dependency of power consumed and heat emanated (by the biochip) on utilization percentages has been presented in SM 2.

### III. POC SYSTEM DESIGN AND IMPLEMENTATION

A POC system for biosensing and biotelemetry was designed and implemented in this work. An illustration of the setup is shown in Fig. 6. At the heart of the setup is an

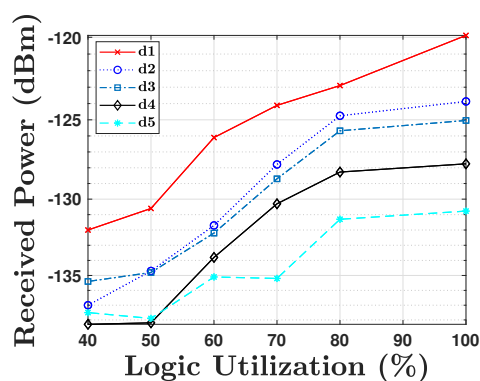


Fig. 5: Received power at various logic utilization for tag-reader separation distances.

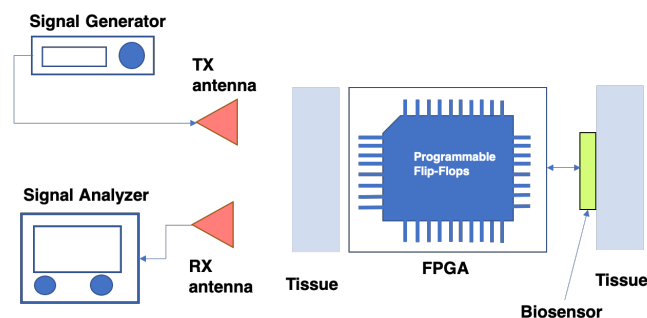


Fig. 6: POC system for biosensing and biotelemetry.

Altera DE0-Cyclone V FPGA chip used as the RFID tag, while two double ridge ultrawideband (0.7 – 18 GHz) horn antennas (Com-Power AH-118) with directional gain of 10 dBi were used as the reader/interrogator in this setup. A Keysight E8257D PSG Analog signal generator with an output power of 15 dBm was used as the signal source while an Agilent MXA N9020A vector signal analyzer was used to record the received (backscattered) waveform. Our system was designed to operate at the 900 MHz Industrial, Scientific and Medical (ISM) band with the frequency ( $f_c$ ) of the incident carrier set to 915 MHz while the modulation frequency is set to 900 kHz. Note that these frequency values were chosen to maximize penetration through biological tissues. Also, the safety standard for in-body transmission allows up to a 28 dBm power limit at frequencies around 1 GHz. Therefore, in adherence to this, the output power limit of our system was restricted to 15 dBm.

Note that General Purpose Input/Output (GPIO) pins (commonly used on integrated circuits to facilitate connections with auxiliary components) as well as conductive traces connecting these pins to the biochip could act as active radiators, however, these pins were usually deactivated before backscattering in our system. This ensured that the backscatter/reflection observed is primarily caused by the biochip and not by an external radiator.

To showcase the capability of our system for realistic vital sign acquisition and communication, we included a biosensor (as shown in Fig. 6) to gather and report the temperature of biomaterials in this work. The temperature sensor used is an

Adafruit MCP9808 High Accuracy I2C Temperature Sensor. This device is capable of sensing temperature between  $-40^{\circ}\text{C}$  to  $+125^{\circ}\text{C}$  with  $\pm 0.25^{\circ}\text{C}$ . An I2C communication interface was used for data transfer from this sensor's output to the FPGA's GPIO pins.

#### IV. LIMITATIONS OF OUR WORK

Although this study is, to the best of our knowledge, the first of its kind, we acknowledge some factors that could preclude its direct deployment into biomedical devices. These limiting factors stem from our use of generic Over-the-Counter (OTA) components such as the FPGA chip. It is important to note that the FPGA chip was used simply to satisfy a proof-of-concept design. We believe that these issues can be easily resolved by porting the outcome of this work into a custom ASIC. Some of these issues merits a discussion.

##### A. Device Size

The size of the FPGA chip used in this work is  $2.1 \times 2.1 \times 0.2$  cm. This can be considered large for bioimplant applications. This issues can be easily abated with a small-sized custom ASIC designed to fit a miniaturized bioimplant.

##### B. Device Power

The high power requirement of the FPGA chip used in this work constitutes a limiting factor. The FPGA chip consumes about 663 mW of power at 40% logic utilization and about 1071 mW at 100% logic utilization (see supplementary note (SM1)). These power values are excessive and could put a strain on the biomedical device's power source. This concern can also be easily abated with the use of a low-power custom ASIC, which will be developed in a future work.

#### V. PROPAGATION MEASUREMENT THROUGH TISSUES

In this section, we present details about the different backscatter measurements conducted with our POC system and the results obtained from propagation through different tissues. Note that for these propagation experiments, the biosensor unit was deactivated such that the resource allocation on the biochip was set to 100% logic utilization i.e., mainly for backscattering.

The measurements were conducted at the EMC<sup>2</sup> indoor lab facility housed in the Technology Square Research Building (TSRB) – a building adjacent to the campus of Georgia Institute of Technology in Atlanta, GA, USA. The indoor lab is a  $11 \times 8.5 \times 4.8$  m room mostly populated with workbenches, chairs, test and measurement equipment (digital sampling oscilloscope, vector network analyzers etc..) and cabinets for storing equipment. The measurements in this work were conducted in a secluded area in the lab with minimal likelihood of Electromagnetic (EM) wave reflectors or scatterers. An initial spectrum scan was conducted to make sure that there were no interfering signals in the channel. To aid positioning of the biological tissue and distance measurements, the measurement setup was placed on a table as shown in Fig 7. For each measurement conducted, the tissue was placed in front of the tag to

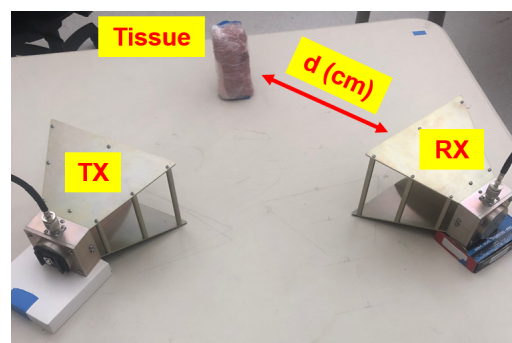


Fig. 7: Measurement setup with varying distances between tag-tissue combination and interrogator (TX - RX antennas).

emulate the tag as a bioimplant embedded in a tissue. This tag-tissue combination will hence be referred to as TTC in this work. Multiple measurements were conducted such that the TX antenna (i.e. source in the interrogator) was fixed at a 25 cm distance from the TTC, while the RX antenna (receiver in the interrogator) was placed so as to create variable distances from the TTC. Note that the choice of interrogator (TX/RX antennas) proximity to the tag stems from our desire to have the system operate in far-field (for a plane-wave assumption) and the corresponding dimension of (broadband) antenna used. A narrowband<sup>1</sup> smaller-sized antenna with a gain of 10 dBi would afford a shorter proximity, which in turn would increase the power of the received signal. For comparability of results, the same locations (with constituents unchanged) were used for measurements with different biological tissues.

It is important to note that occasional temporal variation can be expected in body-centric wireless channels. This variation can be attributed to involuntary movements of internal organs that control activities such as breathing and bowel movements thereby leading to skin pulsation. Also, the human subject's motion can result in temporal variation of the wireless channel and cause a change in orientation of the biotelemetry system. The consequence of the orientation change in an ingestible biotelemetry system is manifested in the form of polarization shift and pathloss increase (a discussion on this has been presented in SM 4). Although we recognize that accounting for the impact of temporal variation is important as this could have an adverse effect on the system's performance, however, given that our objective is to establish a proof-of-concept, a key assumption in our measurement is that the backscatter channel is *quasi-static*. This assumption is fulfilled if there are no vibrations or moving scatterers in the environment, we therefore, made sure of this in our experiment.

##### A. Propagation Measurement With Select Tissues

We conducted propagation measurements with consideration for different types of tissues such as *Skin, Fat and Muscle* (and combinations thereof). These tissues were selected to emulate constituent tissue compositions at probable locations in the body (such as underneath the skin, deep tissue, etc..) in

<sup>1</sup>The narrow-bandwidth of the antenna will be centered at the carrier frequency of the impinging continuous waveform.

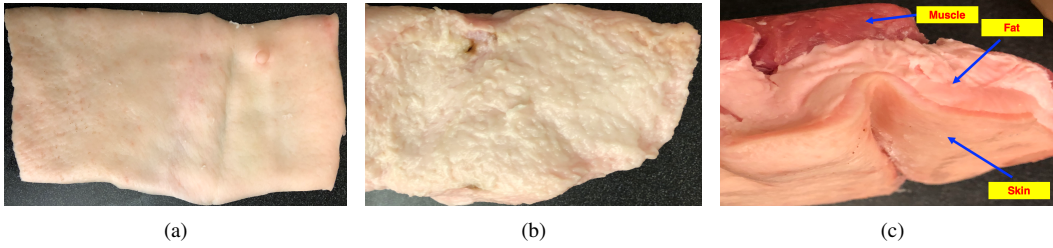


Fig. 8: (a) Skin tissue (b) Fat tissue (c) Skin-Fat-Muscle (SFM) tissue combination.

which bioimplants could be deployed. The tissues used for the various experiments have been grouped into configurations and listed in Table II, while pictures showing some of the different tissues used have been provided in Figs. 8(a) - 8(c).

TABLE II: Tissues configuration.

Configuration	Tissues	Thickness (cm)
1	Without biomaterial	N/A
2	Skin	0.3
3	Fat	2.0
4	Muscle	1.3
5	Skin-Fat-Muscle (SFM)	4.0

We performed the backscatter propagation measurements using the setup described in Fig. 7 with the TTC and (RX) interrogator placed at select separation distances. For the backscattering measurements<sup>2</sup> conducted, the recorded data structure of the power of the backscattered waveform can be represented as  $P_{RX}^{\zeta,v}$ , where  $\zeta \in [1, \dots, 4]$  denotes the indexes of the distances measured such that  $d_\zeta \in [25, 35, 45, 55]$  cm, while  $v = [1, \dots, 5]$  represents the tissue configuration used for the TTC. A model for the distance-dependent received (backscattered) power and shadowing (power-variation) gain are subsequently presented.

1) **Received Power Model:** With consideration for parameters  $\zeta$  and  $v$ , the received power from the empirical data can be modeled as:

$$P_{RX}^{\zeta,v} = P_0^v \cdot \left(\frac{d_\zeta}{d_0}\right)^{\gamma_v} \cdot S_{\sigma}^{\zeta,v} \quad (1)$$

where  $P_0$  is the power received at the reference distance,  $d_0$  (chosen as 25 cm),  $\gamma$  is the pathloss exponent, and  $S_\sigma$  is a random variable describing the power variation i.e., shadowing gain in the environment.

The received power from the various TTC - (RX) interrogator separation distance measurements are shown in the scatter plot presented in Fig. 9. A linear regression fit for the scatter plot shows a monotonic (decrease) dependence of the received power on distance. This decrease can be attributed to a combination of the pathloss in the propagation channel and attenuation by the tissue. Note that any loss incurred from reflection off the tag has been factored into the propagation

<sup>2</sup>It is important to note that for these measurements, the receiver sensitivity on the spectrum analyzer was set to  $S_{\min} = KTB$  (dBm) + NF (dB) + SNR<sub>min</sub>(dB) = -174 dBm + 11 dB + 3 dB = -160 dBm, where  $K$  is the thermal noise power,  $B$  is the receiver bandwidth (Hz), NF is the noise figure and SNR<sub>min</sub> is the minimum Signal-to-Noise Ratio (SNR) allowable on the spectrum analyzer for detection.

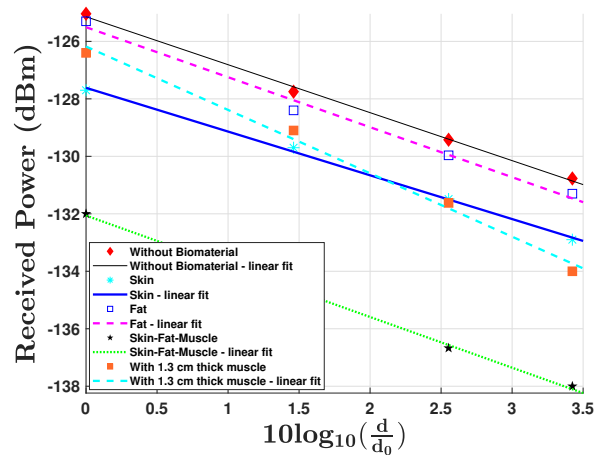


Fig. 9: Linear regression fit for the received power over distance with different tissues structure.

channel loss as the tag is deemed as part of the propagation channel in this work. Values of parameters such as  $P_0$  and  $\gamma$  extracted through a linear fit on the empirical data have been provided in Table III.

TABLE III: Extracted propagation parameters.

Configuration	$P_0$ (dBm)	$\gamma$	$\sigma_{S_\sigma}$ (dB)
1	-125.14	-1.66	0.15
2	-127.61	-1.52	0.12
3	-125.50	-1.73	0.31
4	-126.19	-2.23	0.31
5	-132.05	-1.75	0.08

From the results presented in Table III and Fig. 9, it can be observed that the received power ranges from -125.14 dBm to -130.9 dBm over the distances measured in the experiment conducted without biomaterial – i.e. free-space. It can also be observed that propagation through the fat tissue is close to the case without biomaterial – an occurrence, which has also been observed in measurements conducted in [6]. The tissue combination comprising of Skin-Fat-Muscle (SFM) exhibits the most loss with received power ranging from -132.05 dBm to -138 dBm over the distances measured.

2) **Shadowing Gain:** Shadowing gain (denoted as  $S_\sigma$  in (1)) was obtained by computing the deviation of the received power ( $P_{RX}$ ) at each measured location from the linear regression fit in Fig. 9. As done in other bio-related wireless propagation works such as [25], we modeled the logarithmic

equivalent of the extracted shadowing gain as a zero-mean Gaussian distribution  $\mathcal{N}(0, \sigma_{S_\sigma}(\text{dB}))$ , with the standard deviation (std. dev.) parameter  $\sigma_{S_\sigma}$  provided in Table III. It can be observed from the results presented in Table III that the shadowing gain values are generally small, but nevertheless indicates the impact that the backscatter environment has on the received signal.

### B. Propagation Measurements With Gastrointestinal Tissues

The GI tract (or alimentary canal) comprises of several organs, which includes the stomach, small and large intestines as shown in Fig. 10. The GI tract is unique in its structural form and composition in terms of its multi-layer tissues and fluids present in the stomach and intestines. These compositions will have an impact on data communication (by any ingestible device or bioimplant) from inside the GI tract to outside of the body. If backscattering is to be used for the data communication, then it suffices that backscatter propagation in GI tracts be characterized while taking tissues and GI fluids into consideration.

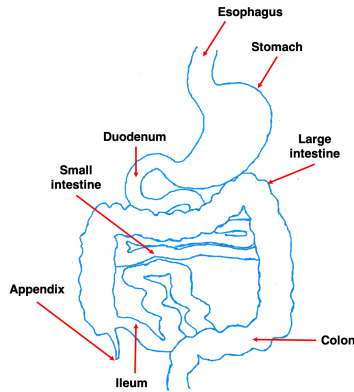


Fig. 10: Gastrointestinal tract with constituent organs.

1) **Gastrointestinal Fluids:** To simulate the chemical composition of the contents of the stomach and the intestines, we created synthetic gastric and intestinal fluids using the procedure proposed in [26].

- **Synthetic Gastric Fluid (SGF) Preparation:** The SGF was produced by combining 2 g of Sodium Chloride (NaCl) with 7 ml of 37% Hydrochloric (HCl) acid and diluted to 1000 ml with distilled, deionised water as done in [26]. We then added 3.2 g/l of pepsin (an enzyme from porcine gastric mucosa) an hour before the SGF was used in our experiment. The measured pH value of the SGF was 1.2.
- **Synthetic Intestinal Fluid (SIF) Preparation:** The SIF was produced by combining 6.8 g of monopotassium phosphate ( $\text{KH}_2\text{PO}_4$ ) with 190 ml of 0.2 N NaOH (used for controlling the pH value) and diluted to 1000 ml with distilled, deionised water. We then added 10 g/l of pancreatin (an enzyme from porcine pancreas) an hour before starting our experiment as suggested in [26]. The pH value of the SIF was 7.4.
- **Gastrointestinal Volume Content States:** According to [27], the human stomach and small intestines have two

volume content states i.e., the *fasted* and *fed* states. The fasted stomach usually contains about 35 ml of resting liquid while fed stomach contains about 242 ml. The fasted state of the small intestine usually contains about 43 ml of liquid while the fed contains about 94 ml. Using this information, the backscattering measurements through the GI tract were conducted with consideration for the fasted and fed GI states.

A combination of Skin, Fat and Muscle (SFM, see Fig. 8(c)) tissues was used to approximate the GI tissues in our experiment. Note that the propagation measurements were conducted by combining a plastic bag containing the GI fluids with the SFM tissues to assemble either a SFM-SGF-tag or SFM-SIF-tag combination, while the (RX) interrogator was placed at varying distance separations from the aforesaid assemblage.

The data structure of the received power from the GI measurements can be represented as  $\hat{P}_{\text{RX}}^{\zeta, \hat{v}_i}$ , where  $\iota \in [1, 2]$  denotes the fasted and fed stomach and intestine states.  $\hat{v}_i \in [1, \dots, 4]$  denotes the index of the GI content and tissue composition such that  $\hat{v}_i = 1$  corresponds to SGF only,  $\hat{v}_i = 2$  corresponds to SIF only,  $\hat{v}_i = 3$  indicates the combination SGF-SFM while  $\hat{v}_i = 4$  indicates the combination of SIF and SFM accordingly.  $\zeta = [1, \dots, 4]$  denotes the indexes of the distances in this case such that  $d_\zeta = [25, 35, 45, 55]$  cm.

2) **Received Power Model:** From the measured data, the received power at different distances was modeled as:

$$\hat{P}_{\text{RX}}^{\zeta, \hat{v}_i} = \hat{P}_0 \cdot \left(\frac{d_\zeta}{d_0}\right)^{\hat{\gamma}_v} \cdot \hat{S}_\sigma^{\zeta, \hat{v}_i} \quad (2)$$

where  $\hat{P}_0$  is the power received at the reference distance of  $d_0$  (chosen as 25 cm),  $\hat{\gamma}$  is the pathloss exponent, and  $\hat{S}_\sigma$  is a random variable describing the power variation i.e., shadowing gain in the environment. A sample scatter plot

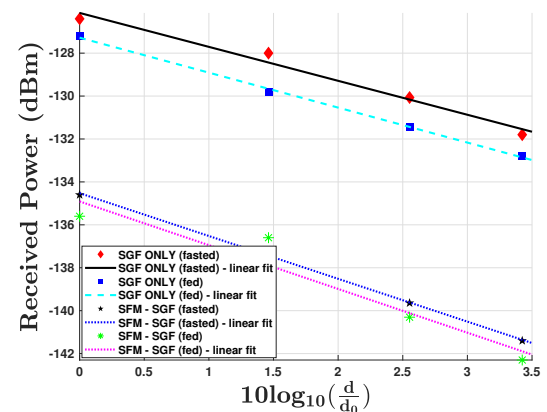


Fig. 11: Linear regression fit of the received power over distance for SGF measurements.

of the received power over the distances measured for the SGF experiment is presented in Fig. 11. Linear regression fits for the scatter plot shows a monotonic (decrease) dependence of the received power on distance for the various scenarios. Values of parameters such as  $\hat{P}_0$  and  $\hat{\gamma}$  extracted through a

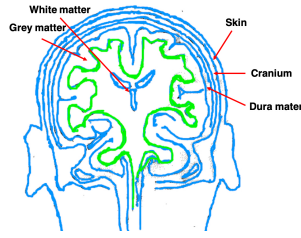


Fig. 12: Head tissue layers.

linear fit for all the measurements related to the GI tract have been provided in Table IV.

TABLE IV: Extracted parameters from GI measurements.

Configuration	$\tilde{P}_0$ (dBm)	$\tilde{\gamma}$	$\tilde{\sigma}_{S_\sigma}$ (dB)
SGF (fasted)	-126.13	-1.60	0.40
SGF (fed)	-127.27	-1.62	0.12
SFM - SGF (fasted)	-134.52	-1.99	0.12
SFM - SGF (fed)	-134.90	-2.00	1.07
SIF (fasted)	-126.07	-1.60	0.48
SIF (fed)	-126.23	-1.60	0.40
SFM - SIF (fasted)	-132.87	-2.10	0.65
SFM - SIF (fed)	-135.74	-2.10	0.38

3) **Shadowing Gain:** We modeled the logarithmic equivalent of the extracted shadowing gain as a zero-mean Gaussian distribution here as well with the std. dev. parameter  $\tilde{\sigma}_{S_\sigma}$  provided in Table IV.

From the results presented in Table IV, it can be observed that the received power in the fed state incurred an additional loss of approximately 0.4 dB than the fasted state in the gastric fluid case while an approximate difference of about 3 dB was observed in the intestinal fluid case.

### C. Propagation Measurement With Neural Tissues

The human head is made up of multiple tissue layers, which includes the skin, cranium (skull bone), dura mater (a membrane layer enveloping the brain), grey matter and white matter as shown in Fig. 12. There has been an increase in research into telemetry from brain implants, with works such as [15], [16] proposing a passive backscattering option due to the thermal sensitivity of brain tissues [28]. To contribute to the on-going neural biotelemetry research, we test the feasibility of our backscatter measurement setup for neural biotelemetry by performing *in-vitro* propagation measurements through a self-developed multi-layer head phantom tissues.

1) **Head Phantom Tissue Development:** Using the head phantom formula presented in [15] and [29], we developed a four layered tissue combination that comprises of the white matter, grey matter, cranium and skin tissues. For ease of experimental test, the dura mater and grey matter layers were combined as one as done in [15] and [16]. The chemicals used for the phantom tissue development are polyethylene powder, NaCl, agar, boric acid, TX-151 and deionized water. The mixture percentages of these chemicals have been presented in the supplementary notes (see SM3). The developed head phantom tissue combination along with actual tissue dimensions used in our work are shown in Figs. 13(a) and 13(b). Note that

the texture of each phantom tissue varies. This disparity can be attributed to the composition of the chemicals in each tissue. Also, the relative permittivity and conductivity of each tissue differ, with polyethylene powder and sodium chloride (NaCl) being used to adjust the phantom's permittivity and conductivity so as to ensure its similarity to human brain tissues. Self-shaping was made possible with agar, while TX-151 was used to increase the mixture's viscosity. Boric acid was finally added as a preservative.



Fig. 13: (a) Head phantom tissue combination (b) dimensions of tissue combination used for the measurement.

For the backscatter measurements conducted, the tag was placed between the grey and white matter (to simulate an implant inserted into the grey matter) with measurements conducted at various TTC - (RX) interrogator separation distances – as done in previous measurements. The recorded data structure of the received power can be represented as  $\tilde{P}_{RX}^\zeta$ , where  $\zeta \in [1, \dots, 4]$  denotes the indexes of the distances measured such that  $d_\zeta \in [25, 35, 45, 55]$  cm.

2) **Received Power Model:** A model for the received power as a function of distance and the shadowing (power-variation) gain can be expressed as:

$$\tilde{P}_{RX}^\zeta = \tilde{P}_0 \cdot \left(\frac{d_\zeta}{d_0}\right)^{\tilde{\gamma}} \cdot \tilde{S}_\sigma^\zeta \quad (3)$$

where  $\tilde{P}_0$  is the power received at the reference distance of  $d_0$  (chosen as 25 cm),  $\tilde{\gamma}$  is the pathloss exponent, and  $\tilde{S}_\sigma$  is the shadowing gain in the environment. A scatter plot of the received power over the distances measured has been provided in SM 7 (due to lack of space). A linear regression fit on the aforementioned scatter plot shows a monotonic (decrease) dependence of the received power on distance while extracted parameters such as  $\tilde{P}_0$  and  $\tilde{\gamma}$  have been provided in Table V.

TABLE V: Extracted Parameters from neural measurements.

Configuration	$\tilde{P}_0$ (dBm)	$\tilde{\gamma}$	$\tilde{\sigma}_{S_\sigma}$
Neural tissues	-127.05	-2.14	0.89

3) **Shadowing Gain:** We modeled the logarithmic equivalent of the extracted shadowing gain here also as a zero-mean Gaussian distribution in the neural tissue measurement with the std. dev. parameter  $\tilde{\sigma}_{S_\sigma}$  provided in Table V.

It can be observed from the result presented in Table V that the received power in the neural measurement is lower than that from the measurement conducted without biomaterial (see Table III) as the magnitude of the decay components of the former significantly exceeds that of the latter.

Note that we also investigated the Specific Absorption Rate (SAR) of our POC system. Results for this investigation has been provided in supplementary note SM3.

## VI. BACKSCATTER COMMUNICATION AND SENSING

Our objective in this section is to conduct high-data-rate communication through tissues using our system while maintaining a high signal fidelity. To achieve this objective, we introduce a channel coding technique along with a signal detection scheme tailored towards backscatter applications and then conducted biotelemetry measurement by relaying information (tissue temperature results) garnered from an implanted biosensor to the interrogator.

### A. Backscatter Channel Coding Design

Temporal variation, interference, noise and multipath components (MPCs) in the propagation channel often lead to low signal fidelity in wireless communications. The low signal fidelity manifests itself in the form of a low Bit-Error-Rate (BER) in the digital data transmission. Channel coding is often employed as a technique for alleviating low Bit-Error-Rate (BER) in data communication. Coding has been introduced in body-related wireless applications due to the non-static nature of the human body while signals from bioimplants could also be corrupted by unknown and modulated ambient signals, which could make reliable detection a challenging problem.

There have been several coding schemes used for traditional RFID backscatter applications in the literature. These coding schemes include Non-Return-to-Zero (NRZ), Miller coding, Return-to-Zero (RZ), Manchester and Unipolar. The Manchester coding will be adopted in this work.

Manchester Coding (MC) is a phase encoding method to create a simple block code that maps 0 into 10 and 1 into 01 from an original data stream to an equivalent (encoded) data stream. In this procedure, the first and second half of the Manchester code associated with the  $\epsilon$ -th original data symbol  $\Gamma_\epsilon$  have been depicted in Fig. 14 as  $\Delta_\epsilon^\alpha$  and  $\Delta_\epsilon^\beta$ .

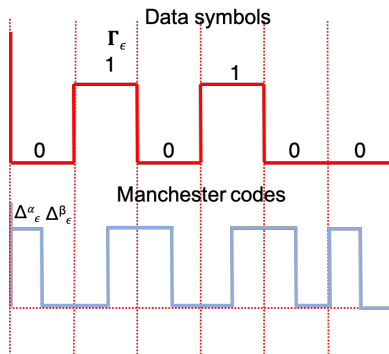


Fig. 14: Data symbols and equivalent Manchester codes.

### B. Backscatter Signal Detector Design

The backscatter signal detector used in this work is a modified<sup>3</sup> version of the semi-coherent Manchester coding

<sup>3</sup> The modification involves simplifying the SeCoMC detector towards a bistatic RFID setup while providing a means to extract parameter estimates pertinent to the detector's performance assessment.

(SeCoMC) detector presented in [30]. The modified SeCoMC is a low-latency, energy efficient detector, which eliminates the requirements of estimating decision threshold and enables immediate symbol-by-symbol detection. The derivation of the modified SeCoMC detector in terms of its decision rule, training algorithm for feasibility and parameter estimation as well as its performance assessment are subsequently discussed below.

1) **Decision Rule Derivation for the Detector:** With the setup shown in Fig. 7, a mathematical description of the backscatter communication can be expressed such that the signal from the source (TX antenna) of the interrogator to the tag can be represented as

$$x_s[n] = h_{st}s[n], \quad (4)$$

where  $s[n]$  is the signal from the source and  $h_{st}$  is the channel coefficient between the source and tag. The signal backscattered by the tag to the received (RX antenna) can be represented as:

$$y[n] = h_{tr}\Delta[n]x_s[n] + w[n], \quad (5)$$

where  $h_{tr}$  is the channel coefficient between the tag<sup>4</sup> and the RX antenna of the interrogator with equiprobable binary symbols from the tag denoted as  $\Delta[n] \in \{0, 1\}$ .  $w[n]$  is the zero mean additive white Gaussian noise ( $\mathcal{N}(0, N_w)$ ) with noise power  $N_w$ .

Using a binary hypothesis testing as a criteria for making decisions, we let  $H_0$  and  $H_1$  represent the two hypothesis associated with the binary symbols  $\Delta = 0$  and  $\Delta = 1$  respectively and then the received signal can be modeled as

$$y[n] = \begin{cases} h_0s[n] + w[n], & H_0, & n = 1 \cdots N_p \\ h_1s[n] + w[n], & H_1, & n = 1 \cdots N_p \end{cases}, \quad (6)$$

where  $h_1 = h_{tr}\Delta[n]h_{st}$ . Note that  $h_0s[n]$  was included in this binary hypothesis testing to help determine the feasibility of our system under certain conditions.

With Manchester coding the received signal (expressed in a vector form) during the  $\epsilon$ -th symbol interval can be expressed as

$$y_\epsilon = \hat{y}_\epsilon^\alpha \hat{y}_\epsilon^\beta, \quad \alpha\beta \in \{01, 10\} \quad (7)$$

while the received signal energy is denoted as:

$$\hat{Z}_\epsilon^j = \|\hat{y}_\epsilon^j\|^2 \quad j \in \{\alpha, \beta\}. \quad (8)$$

In general, the energy  $\mathcal{Z}$  of the received signal is a sufficient statistic for the detection problem as  $\mathcal{Z} = \sum_{n=1}^{N_p} |y[n]|^2$  is a non-central chi-square random variable with  $2N_p$  degrees of freedom. Note that for large  $N_p$  values,  $\mathcal{Z}$  becomes a Gaussian random variable (from central limit theorem) such that the distribution of  $\mathcal{Z}$  under hypothesis  $H_i$  can be written as

$$f_{\mathcal{Z}}(\mathcal{Z}|H_i) = \frac{1}{\sqrt{2\pi\zeta_i}} e^{-\frac{(\mathcal{Z}-\mu_i)^2}{2\zeta_i}} \quad i = 0, 1 \quad (9)$$

<sup>4</sup>Note that any reflection loss from the tag as been abstracted into the channel coefficient since the tag is considered part of the propagation channel in this work.

where  $\mu_i = N_p \sigma_i^2$ ,  $\varsigma_i = 2N_p |h_i|^2 P_s N_w + N_p N_w^2$ . Note that  $\sigma_i^2 = |h_i|^2 P_s + N_w$ . The decision rule is derived such that

$$f_Z(Z|H_1) \geq_{H_0}^{H_1} f_Z(Z|H_0). \quad (10)$$

For the the MC equivalent, we formulate (10) as

$$f_{\hat{Z}_\epsilon}(\hat{Z}_\epsilon^\alpha \hat{Z}_\epsilon^\beta | H_1) \geq_{H_0}^{H_1} f_{\hat{Z}_\epsilon}(\hat{Z}_\epsilon^\alpha \hat{Z}_\epsilon^\beta | H_0) \quad (11)$$

$$f_{\hat{Z}_\epsilon}(\hat{Z}_\epsilon^\alpha | H_0) f_{\hat{Z}_\epsilon}(\hat{Z}_\epsilon^\beta | H_1) \geq_{H_0}^{H_1} f_{\hat{Z}_\epsilon}(\hat{Z}_\epsilon^\alpha | H_1) f_{\hat{Z}_\epsilon}(\hat{Z}_\epsilon^\beta | H_0) \quad (12)$$

which simplifies to a decision rule:

$$\hat{Z}_\epsilon^\alpha \geq_{H_1}^{H_0} \hat{Z}_\epsilon^\beta \quad (13)$$

It can be deduced from (13) that the uniqueness of the detection algorithm with Manchester coding proposed in this work is that a pre-defined or estimated energy level threshold is not needed for comparison with the received signal's energy – as done in traditional detection algorithms since the decision rule of the proposed detection scheme simply compares the received energy between contiguous symbols (mid-bit transition) to infer the original data symbol [30].

### 2) Training for Feasibility and Parameter Estimation:

Without a priori knowledge of the backscattered signal structure or the Channel State Information (CSI), we intend to evaluate the feasibility of the proposed detector and estimate crucial parameters needed for its performance assessment. This will be done by using a training procedure such that a successive number of  $L$  training symbols<sup>5</sup> "1" are appended as preambles to the backscattered data symbol (length  $E$ ) i.e., the payload. The outcome of the training will indicate if the detector will "pass" or "fail" based on the propagation channel conditions and provide estimates for parameter  $\sigma_i^2$ . The training procedure is presented in Algorithm 1 below.

#### Algorithm 1 Training Algorithm

**Input:** The received training signal vectors:  $[y_1; \dots; y_L]$

**Output:** (i) Boolean - Pass or Fail (ii) Values for  $\sigma_0^2$  and  $\sigma_1^2$

- 1: Compute the received signal energy  $\hat{Z}_l^j = \|\hat{y}_l^j\|^2$
- 2: Compute  $\Omega_l = \frac{\sum_{l=1}^L \hat{Z}_l^\alpha}{L \cdot N_p}$ ,  $\Psi_l = \frac{\sum_{l=1}^L \hat{Z}_l^\beta}{L \cdot N_p}$
- 3: Evaluate the relationship between  $\Omega_l$  and  $\Psi_l$
- 4: if  $\Omega_l \geq \Psi_l$  then the detector will fail; exit
- 5: else
- 6: Compute  $\varphi_l = \frac{\|\hat{Z}_l^j\|^2}{N_p}$
- 7: Sort  $\varphi_l$  in ascending order
- 8:  $\bar{\varphi}_l = \text{Sort}\{\varphi_l\}$
- 9: Compute  $\varrho^{\min} = \frac{2}{L} \sum_{l=1}^{L/2} \bar{\varphi}_l$ ,  $\varrho^{\max} = \frac{2}{L} \sum_{l=L/2+1}^L \bar{\varphi}_l$
- 10: Choose a subset  $[y_1; \dots; y_{1 \leq w < L}]$ , of the training bits
- 11: Compute  $\varrho_F = \frac{1}{w} \sum_{l=1}^w \frac{\|\hat{Z}_l^j\|^2}{N_p}$
- 12: if  $|\varrho^{\min} - \varrho_F| < |\varrho^{\max} - \varrho_F|$
- 13: set  $\sigma_0^2 = \varrho^{\max}$  and  $\sigma_1^2 = \varrho^{\min}$
- 14: else set  $\sigma_0^2 = \varrho^{\min}$  and  $\sigma_1^2 = \varrho^{\max}$
- 15: end if
- 16: end if

It is important to note that in Algorithm 1 if  $\Omega_l \geq \Psi_l$  then the detector fails; an outcome that implies the presence of a strong spurious interference in the propagation channel.

<sup>5</sup>Note that the value of  $L$  can be selected based on the data rate constraint.

3) **Detector Algorithm Implementation:** Given the received signal, the transmitted data symbols can be obtained with the aid of the modified SeCoMC algorithm. We summarize the modified SeCoMC detector algorithm as follows:

#### Algorithm 2 Modified SeCoMC Detector

**Input:** The received signal vectors:  $[y_1; \dots; y_L; y_1; \dots; y_\epsilon; \dots; y_E]$

**Output:** The detected symbols:  $[\Gamma_1, \dots, \Gamma_\epsilon, \dots, \Gamma_E]$

- 1: Training phase: invoke Algorithm 1
- 2: For  $\epsilon$  from 1 to  $E$
- 3: compute  $\hat{Z}_\epsilon^\alpha = \|\hat{y}_\epsilon^\alpha\|^2$ ,  $\hat{Z}_\epsilon^\beta = \|\hat{y}_\epsilon^\beta\|^2$
- 4: if  $\hat{Z}_\epsilon^\alpha > \hat{Z}_\epsilon^\beta$ , then let  $\Gamma_\epsilon = 0$ , else  $\Gamma_\epsilon = 1$ , end if
- 5: end if
- 6: end for
- 7: Return  $[\Gamma_1, \dots, \Gamma_\epsilon, \dots, \Gamma_E]$

4) **Performance Assessment of Detector:** The performance of the modified SeCoMC can be expressed in terms of the BER as

$$P_e = \frac{1}{2} \text{erfc} \left( \frac{\sqrt{N_p} | |h_1|^2 - |h_0|^2 |}{2\sqrt{\frac{|h_0|^2 + |h_1|^2}{\varkappa} + \frac{1}{\varkappa^2}}} \right), \quad (14)$$

where  $\varkappa$  denotes the Signal-to-Noise Ratio (SNR). Note that with an assumption of high SNR<sup>6</sup> and large  $N_p$ <sup>7</sup> (14) can be simplified to

$$P_e = \frac{1}{2} \text{erfc} \left( \frac{1}{2} \sqrt{\frac{N_p}{N_w}} |\sigma_0 - \sigma_1| \right) \quad (15)$$

with  $\sigma_0$  and  $\sigma_1$  obtained from Algorithm 1. The application of the proposed detector to biotelemetry measurements will be discussed subsequently.

### C. Biotelemetry Measurement

We conducted a series of biotelemetry measurements to showcase the ability of our proposed system in remote monitoring of vital signs (such as temperature) while transmitting the information in either a single- or multi-bit fashion. Note that for measurements conducted in this section, the biochip logic utilization was distributed such that 80% of the resources was allocated to backscatter communication while the remaining 20% was allocated to sensor data acquisition and processing.

1) **Dynamic Single-bit Measurements:** The dynamic single-bit measurement involves the continuous (real-time) transmission of a single bit, which utilizes the entire 80% logic resource allocated to backscattering at a time. We conducted backscattering measurements<sup>8</sup> through the muscle tissue (using configuration 4 from Table II) with TTC - (RX) interrogator separation distances  $d \in [25, 35, 45, 55]$  cm while using the data sequence structure discussed in Sec. V-B. The data sequence comprises of a preamble – 30 training symbols '1' or '01' (Manchester Coded) and priorly selected data symbol

<sup>6</sup>We consider  $\varkappa > 10$  dB a high SNR case.

<sup>7</sup>Using  $N_p = 30$  can be considered as large. However if the PDF  $f_z(z|H_i)$  is smooth, then the value of  $N_p$  can be as low as 5 [31], [32].

<sup>8</sup>Note that these measurements were conducted in the vector mode of the spectrum analyzer such that  $S_{\min} = \text{KTB (dBm)} + \text{NF (dB)} + \text{SNR}_{\min}(\text{dB}) = -154 \text{ dBm} + 11 \text{ dB} + 3 \text{ dB} = -140 \text{ dBm}$ .

(payload) 1101 or 01011001 (Manchester coded equivalent). The data symbol was repeated 12 times such that  $N_p = 126$  for an entire measurement duration of 62 s. Note that  $f_m$  was set to 900 kHz while the duration of each bit set to 500 ms. It is important to note that the bit duration of 500 ms was arbitrarily chosen. This value can be adjusted to fit the application-data rate need as decreasing this value will significantly increase the data rate. As an illustration, the received data symbols from the

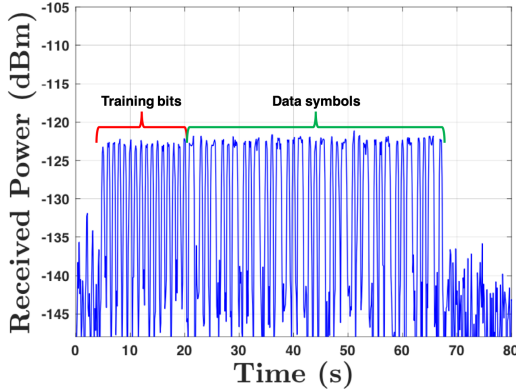


Fig. 15: Single-bit measurement result.

dynamic single bit measurement conducted at arbitrary TTC - (RX) interrogator distance separation of 7.5 cm is presented in Fig. 15 while algorithms 1 and 2 are used to detect the data symbols. The performance of the proposed detector in terms of BER vs SNR for the dynamic single-bit case has been provided in SM6.

2) **Dynamic Multi-bit Measurements:** The dynamic multi-bit measurement in this work involves the continuous transmission of 4-bits at a time such that  $f_m = \{1, 2, 3, 4\} \in [0.900, 0.933, 0.969, 1.049]$  MHz with 20% of logic resources assigned to each bit. Note that modulation frequencies  $f_m$  were arbitrarily selected. The backscattering measurements was conducted using biomaterial from configuration 4 in Table II with priorly selected sequence of  $\{0001, 0001, 1111, 1101\}$ , which were repeated for a measurement duration of 90 s. For illustration purposes, the received data symbols from

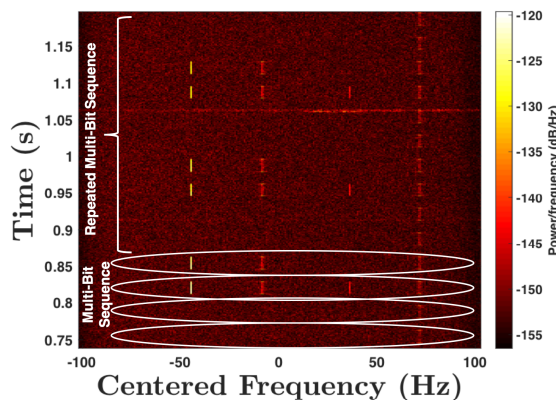


Fig. 16: Multi-bit (4 bits) measurement result.

the dynamic multi-bit measurement conducted at an arbitrary

TTC - (RX) interrogator distance separation of 7.5 cm is presented in Fig. 16. The transmitted bit sequences are clearly observable from Fig. 16 – this validates the capability of our system to performing multi-bit backscatter communication. The performance of the proposed detector in terms of BER vs SNR for the dynamic multi-bit case has been provided in SM6.

### 3) **Dynamic Temperature Measurements With Biosensor:**

A real-time tissue temperature measurement was conducted using the dynamic single-bit approach with our backscatter setup and a temperature measuring biosensor. The configuration of this measurement setup is similar to that provided in Fig. 6. Note that a muscle tissue from Configuration 4 was used for this experiment. The initial temperature of the muscle tissue was 22° C, however, after about 48 s of continuously measuring the tissue’s temperature, a block of ice was placed on the tissue to vary its temperature – thereby bring the tissue’s temperature to 16° C. This temperature change affords us the opportunity to test the real-time dynamic measurement capability of our system. The received data from the dynamic temperature measurement at an arbitrary distance has been provided in Fig. 17.

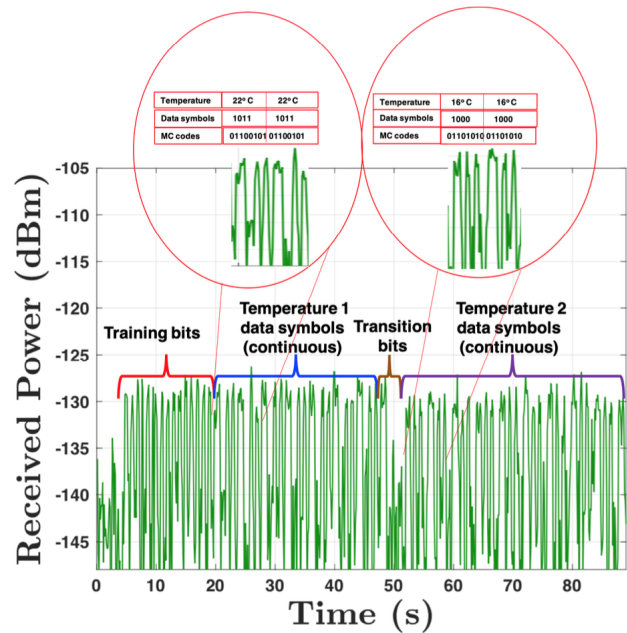


Fig. 17: Temperature measurement result from biosensor.

It is clearly observable that the data symbols from the two different temperatures measured i.e., Temperature 1 (22° C) and Temperature 2 (16° C) are clearly resolvable. Note that a temperature change interrupt configured into the biochip required a manual triggering, at the time the block of ice was introduced for a tissue temperature change. This resulted into the “transition bits” shown in Fig. 17. Although the use of a manual interrupt was unavoidable as this is a POC setup, nevertheless, the occurrence of errant bits – branded as “transition bits” – did not compromise the real-time capture of the tissue temperatures as we were able to continuously measure the Temperature 2 (16° C) for the remaining 38 s duration of the experiment.

## VII. SUMMARY AND CONCLUSION

We have successfully conducted biotelemetry through biological and phantom tissues with a self-developed POC system, which uses transistor switching in an ASIC (FPGA chip) in place of a traditional RFID system for backscatter communication. Our proposed POC is antenna-less, frontend-less, flexible, versatile and is an improvement on state of art in RFID backscatter communication. We showed that backscattered waveforms from our system can penetrate tissues of various compositions, thicknesses and fluids (GI contents) with power received at distances of up to 55 cm away from the tag. We also provided propagation channel parameters and statistical models that can be used predict received (backscattered) power at various distances. Results from the single- and multi-bit biotelemetry measurements showed a good received signal fidelity with low BER while also being able to resolve varying tissue temperatures measured by a biosensor in a dynamic fashion. There were limitations to the system presented in this work. These limitations primarily stems from our use of OTA components in the POC assembly. These limitations can be easily abated with the use of a custom ASIC that will be developed in a future work. It is noteworthy that although our work can be modified to accommodate simultaneous wireless power transfer (in addition to backscatter communication), however, using the design as presented in this paper for simultaneous wireless power transfer would result in considerable power inefficiency – yielding a low received power. This stems from the impedance mismatch created as a result of the two state RF loads i.e. changing impedance at the implant side. Overall, this work will aid the design and development of biosensing and biotelemetry devices.

## REFERENCES

- [1] M. K. Goenka, S. Majumder, and U. Goenka, "Capsule endoscopy: Present status and future expectation," *World Journal of Gastroenterology: WJG*, vol. 20, no. 29, p. 10024, 2014.
- [2] Zhang, Shiyi and *et al.*, "A pH-responsive supramolecular polymer gel as an enteric elastomer for use in gastric devices," *Nature materials*, vol. 14, no. 10, p. 1065, 2015.
- [3] Verma, Malvika *et al.*, "A gastric resident drug delivery system for prolonged gram-level dosing of tuberculosis treatment," *Science translational medicine*, vol. 11, no. 483, p. eaau6267, 2019.
- [4] R. J. Coffey, "Deep brain stimulation devices: a brief technical history and review," *Artificial organs*, vol. 33, no. 3, pp. 208–220, 2009.
- [5] R. E. Hampson *et al.*, "Developing a hippocampal neural prosthetic to facilitate human memory encoding and recall," *Journal of neural engineering*, vol. 15, no. 3, p. 036014, 2018.
- [6] D. Vasisht, G. Zhang, O. Abari, H.-M. Lu, J. Flanz, and D. Katabi, "In-body backscatter communication and localization," in *Proceedings of the 2018 Conference of the ACM Special Interest Group on Data Communication*. ACM, 2018, pp. 132–146.
- [7] Y. Ma, Z. Luo, C. Steiger, G. Traverso, and F. Adib, "Enabling deep-tissue networking for miniature medical devices," in *Proceedings of the 2018 Conference of the ACM Special Interest Group on Data Communication*, 2018, pp. 417–431.
- [8] D. R. Agrawal *et al.*, "Conformal phased surfaces for wireless powering of bioelectronic microdevices," *Nature biomedical engineering*, vol. 1, no. 3, p. 0043, 2017.
- [9] H. Cao *et al.*, "An implantable, batteryless, and wireless capsule with integrated impedance and pH sensors for gastroesophageal reflux monitoring," *IEEE Transactions on Biomedical Engineering*, vol. 59, no. 11, pp. 3131–3139, 2012.
- [10] H. Cao, S. Rao, S.-j. Tang, H. F. Tibbals, S. Spechler, and J.-C. Chiao, "Batteryless implantable dual-sensor capsule for esophageal reflux monitoring," *Gastrointestinal endoscopy*, vol. 77, no. 4, pp. 649–653, 2013.
- [11] A. K. RamRakhyani, S. Mirabbasi, and M. Chiao, "Design and optimization of resonance-based efficient wireless power delivery systems for biomedical implants," *IEEE Transactions on Biomedical Circuits and Systems*, vol. 5, no. 1, pp. 48–63, 2010.
- [12] R. Das, F. Moradi, and H. Heidari, "Biointegrated and wirelessly powered implantable brain devices: A review," *IEEE Transactions on Biomedical Circuits and Systems*, vol. 14, no. 2, pp. 343–358, 2020.
- [13] M. Schormans, V. Valente, and A. Demosthenous, "Practical inductive link design for biomedical wireless power transfer: A tutorial," *IEEE Transactions on Biomedical Circuits and Systems*, vol. 12, no. 5, pp. 1112–1130, 2018.
- [14] P. Nadeau *et al.*, "Prolonged energy harvesting for ingestible devices," *Nature Biomedical Engineering*, vol. 1, pp. 0022 EP –, 02 2017.
- [15] A. Kiourti, C. W. Lee, J. Chae, and J. L. Volakis, "A wireless fully passive neural recording device for unobtrusive neuropotential monitoring," *IEEE Transactions on Biomedical Engineering*, vol. 63, no. 1, pp. 131–137, 2015.
- [16] H. N. Schwerdt, F. A. Miranda, and J. Chae, "Wireless fully passive multichannel recording of neuropotentials using photo-activated rf backscattering methods," *IEEE Transactions on Microwave Theory and Techniques*, vol. 63, no. 9, pp. 2965–2970, 2015.
- [17] C. Cheng, L. N. Nguyen, M. Prvulovic, and A. Zajić, "Exploiting Switching of Transistors in Digital Electronics for RFID Tag Design," *IEEE Journal of Radio Frequency Identification*, vol. 3, no. 2, pp. 67–76, June 2019.
- [18] W. Jeon, J. Melngailis, and R. W. Newcomb, "Disposable cmos passive rfid transponder for patient monitoring," in *2006 IEEE International Symposium on Circuits and Systems*. IEEE, 2006, pp. 4–pp.
- [19] T. Inaba, "Value of sparse rfid traceability information in asset tracking during migration period," in *2008 IEEE International Conference on RFID*. IEEE, 2008, pp. 183–190.
- [20] M. Baghaei-Nejad, D. S. Mendoza, Z. Zou, S. Radiom, G. Gielen, L.-R. Zheng, and H. Tenhunen, "A remote-powered RFID tag with 10Mb/s UWB uplink and- 18.5 dBm sensitivity UHF downlink in 0.18  $\mu$ m CMOS," in *2009 IEEE International Solid-State Circuits Conference-Digest of Technical Papers*. IEEE, 2009, pp. 198–199.
- [21] A. Lazaro, A. Ramos, R. Villarino, and D. Girbau, "Active uwb reflector for rfid and wireless sensor networks," *IEEE Transactions on Antennas and Propagation*, vol. 61, no. 9, pp. 4767–4774, 2013.
- [22] T. Karacolak, R. Cooper, E. S. Unlu, and E. Topsakal, "Dielectric properties of porcine skin tissue and in vivo testing of implantable antennas using pigs as model animals," *IEEE Antennas and Wireless Propagation Letters*, vol. 11, pp. 1686–1689, 2012.
- [23] H. Stockman, "Communication by means of reflected power," *Proceedings of the IRE*, vol. 36, no. 10, pp. 1196–1204, 1948.
- [24] C.-L. Cheng, S. Sangodoyin, L. N. Nguyen, M. Prvulovic, and A. Zajić, "Digital Electronics as RFID Tags: Impedance Estimation and Propagation Characterization at 26.5 GHz and 300 GHz," *IEEE Journal of Radio Frequency Identification*, vol. 5, no. 1, pp. 29–39, 2021.
- [25] S. Sangodoyin and A. F. Molisch, "Impact of Body Mass Index on Ultrawideband MIMO BAN Channels—Measurements and Statistical Model," *IEEE Transactions on Wireless communications*, vol. 17, no. 9, pp. 6067–6081, 2018.
- [26] T. Egan, J.-C. Jacquier, Y. Rosenberg, and M. Rosenberg, "Cold-set whey protein microgels containing immobilised lipid phases to modulate matrix digestion and release of a water-soluble bioactive," *Journal of Microencapsulation*, vol. 31, no. 2, pp. 184–192, 2014.
- [27] D. M. Mudie *et al.*, "Quantification of gastrointestinal liquid volumes and distribution following a 240 ml dose of water in the fasted state," *Molecular pharmaceuticals*, vol. 11, no. 9, pp. 3039–3047, 2014.
- [28] S. F. Owen, M. H. Liu, and A. C. Kreitzer, "Thermal constraints on in vivo optogenetic manipulations," *Nature neuroscience*, vol. 22, no. 7, pp. 1061–1065, 2019.
- [29] K. Ito, K. Furuya, Y. Okano, and L. Hamada, "Development and characteristics of a biological tissue-equivalent phantom for microwaves," *Electronics and Communications in Japan (Part I: Communications)*, vol. 84, no. 4, pp. 67–77, 2001.
- [30] Q. Tao, C. Zhong, H. Lin, and Z. Zhang, "Symbol detection of ambient backscatter systems with manchester coding," *IEEE Transactions on Wireless Communications*, vol. 17, no. 6, pp. 4028–4038, 2018.
- [31] J. Qian, F. Gao, G. Wang, S. Jin, and H. Zhu, "Semi-coherent detection and performance analysis for ambient backscatter system," *IEEE Transactions on Communications*, vol. 65, no. 12, pp. 5266–5279, 2017.
- [32] A. Papoulis and S. U. Pillai, *Probability, random variables, and stochastic processes*. Tata McGraw-Hill Education, 2002.